A hybrid experimental-computational approach for predicting Ti-6Al-4V powder degree of spheroidization using artificial neural networks

Justin Mbwebwe[1*], *Andrei* Kolesnikov[1], *Lucey* Mavhungu[1] and *Hertzog* Bissett[2]

[1]Department of Chemical, Metallurgical and Materials Engineering, Tshwane University of Technology, Pretoria 0185, South Africa
[2]The South African Nuclear Energy Corporation SOC Ltd. (Necsa), Elias Motsoaledi Street Extension (Church Street West) R 104 Pelindaba, Madibeng Municipality, North West Province, 0240, South Africa

Abstract. A hybrid experimental-computational method was designed to predict the spheroidicity of Ti-6Al-4V powder processed through the radio frequency plasma spheroidization process. Twenty-three experimental runs were conducted to measure particle spheroidicity using optical microscopy. A validated computational fluid dynamics model developed in Ansys Fluent was then used to expand the dataset to 67 samples by simulating additional parameter combinations and varying particle size, plasma power, gas flow rate, and powder feed rate. The combined dataset was used to train a feedforward neural network in PyTorch, which showed improved performance with larger training sets. Sensitivity analysis and three-dimensional response surfaces revealed optimal process conditions (12-15 kW power for 60-100 µm powders; 0.6-1.0 kg/h at 40-60 slpm gas flow) to maximize spheroidicity. The hybrid approach proved reliable for predicting spheroidicity and offers actionable guidance for process optimization.

1 Introduction

As technology and manufacturing evolve, pursuing innovative, environmentally friendly, and cost-efficient processes has become critical [1]. Additive manufacturing (AM), or 3D printing, has recently received significant interest due to its distinct advantages over conventional techniques [2], particularly in the automotive and aerospace sectors for the production of lightweight, complex, and customized components, thus enhancing design flexibility and material efficiency [3]. Ti-6Al-4V (Ti64), which accounts for approximately 45% of the total titanium production, has emerged as a material of choice in AM applications due to its high strength-to-weight ratio, corrosion resistance, chemical stability, and biocompatibility [4]. However, the success of AM processes heavily depends on the morphological characteristics of the metal powders used [5]. Particle shape and size distribution are two of the main properties that dictate the consistency and uniformity in

* Corresponding author: justinmbwebwe@gmail.com

powder layering, which are critical for producing high-quality printed parts [6]. Spheroidized powders improve flowability and packing density [7].

Among new technologies, radio frequency (RF) inductively coupled plasma spheroidization appears to be the most promising technique to produce highly spherical Ti-6Al-4V powder, allowing the conversion of irregularly shaped titanium alloy particles into spherical particles with improved flowability, narrow size distribution, and uniform composition [8]. In the RF plasma spheroidization process, powder particles are injected into a high-temperature (up to 10000 K) plasma stream. The high-temperature plasma stream melts the injected powder particles, which are then converted into small droplets under surface tension. Due to gravity, the hot droplets fall towards the spheroidization reactor exit and solidify as the temperature drops. Spheroidized particles are then collected at the bottom of the reactor [9, 10]. However, the quality of the spheroidized powder depends on several operating variables. Plasma operating parameters such as gas composition and flow rate, reactor pressure, and plasma power greatly influence the spheroidization efficiency [11]. But the raw material powder properties, such as powder feeding rate and particle size, are also essential factors having a significant influence on the extent to which the collected powder particles are spheroidized [12].

Existing research has explored the effects of individual parameters on powder spheroidicity. Y.L. Li and T. Ishigaki [13] experimentally investigated the effects of hydrogen addition to the sheath gas and carrier gas velocity on the spheroization ratio of titanium carbide. Several years later, H. Hou *et al* [14] conducted a study on the spheroidization of silica powders, where they not only investigated the effect of the gas flow rate on spheroidization, but also the effect of particle size. Despite the many advances brought about by the studies mentioned above, controlling the spheroidization process performance remains complex due to the many variables to be monitored. In addition, high running costs are involved. Considering these challenges, numerical simulation appears as an alternative method that can be effective, and can be used to describe the intricate spheroidization mechanism and subsequently predict the spheroidization ratio [15]. Multiple computational fluid dynamics (CFD) models of the spheroidization process have been proposed over the recent years, and they have provided insights into thermal histories and particle trajectories during RF plasma processing [16-18].

However, while CFD simulations offer valuable insights into the process, they must be validated against experimental data to assess their accuracy properly [19]. Furthermore, extracting predictive models from these simulations for practical applications can be challenging, as CFD models still have areas of improvement, including physical modelling of turbulence, numerical algorithms, and knowledge extraction [20]. In addition, they struggle to fully account for multi-parameter interactions inherent to dynamic systems, without the involvement of high computational cost. Though efforts are underway to develop novel turbulence models and algorithms to enhance CFD techniques [21], there is growing interest in alternative tools that may either replace or assist CFD simulations for improved accuracy and faster predictions. Artificial intelligence and data-driven models, particularly artificial neural networks (ANNs), have emerged as a viable alternative for modelling and predicting nonlinear processes [22].

ANNs have demonstrated success in predicting material properties. In the early 2000s, S. Calcaterra *et al* [23] demonstrated the ability of ANNs to forecast the tensile properties of spheroidal cast iron. Around the same period, R.P. Cherian *et al* [24] applied ANNs in selecting process parameters for powder metallurgy. More recently, T.A. Choudhury *et al* [25] developed an ANN-based model to predict particle behaviour in atmospheric plasma spray systems. Nevertheless, most of the previous studies share as limitation, the small size of the experimental dataset (less than 20 samples) used to design and train the ANN model. This constrains the development of accurate machine learning models, affecting their

transferability and generalisability abilities [26]. Therefore, there is a critical need to augment experimental data in a manner that retains fidelity to real plasma-particle behaviour while enabling robust ANN training. This study confronts these challenges by proposing a hybrid framework that augments limited experimental data with CFD-generated datasets, facilitating the training of reliable ANNs, particularly for the spheroidicity prediction of Ti-6Al-4V powder.

2 Methodology

A hybrid dataset was created by combining experimental and computational Ti64 spheroidization data. An initial dataset of 23 samples was generated by varying particle size and plasma power while keeping gas flow and powder feed rate constant. This data was used to validate a CFD model designed to simulate the RF spheroidization process, with validation performed by comparing the percentage error between experimental and computational spheroidicity values.

2.1 Experimental data generation

2.1.1 Sample preparation

Commercial Ti64 Grade 23 powder was procured from the Council for Scientific and Industrial Research (CSIR) in Pretoria, South Africa. Before the experimental work, a shaking sieve classified the powder into seven fractions of different sizes, as shown in Table 1. Each powder size class was then characterized using optical microscopy.

Table 1. Particle size distribution of the Ti64 feed powder.

Powder class	1	2	3	4	5	6	7
Particle size (µm)	25-38	45-63	63-75	75-90	90-106	106-125	>125

2.1.2 Experimental set-up and procedure

The experimental facility Teksphero-15, shown in Figure 1(a) and specifically designed for research, was used to spheroidize Ti64 Grade 23 powder. The RF induction coil was connected to a 15-kW power supply. Argon gas was slowly inserted into the RF torch and subjected to a gradual increase in operating pressure and input power until the formation of a thermal plasma. High-purity argon gas was used as both plasma gas and sheath gas. To increase the low enthalpy and heat conductivity of argon gas, the additional gas method used by Z. Karoly and J. Szepvolgyi [27], was applied. Helium was added to the sheath gas in different proportions. On average, the titanium alloy powder was fed through the thermal plasma at a 1 kg/h feed rate. While passing through the high-temperature plasma region, the in-flight powder particles were rapidly heated and melted into liquid droplets. Under surface tension, the metal drops were spontaneously concentrated into spheres. After the required amount of powder was treated, the plasma was extinguished, allowing the reactor to cool down. The spheroidized powder was collected from the collection pot at the bottom of the RF reactor, as shown in Figure 1(b). To generate an experimental dataset, particle size and plasma power were varied in the 25 – 125 µm range and 10 – 15 kW, respectively.

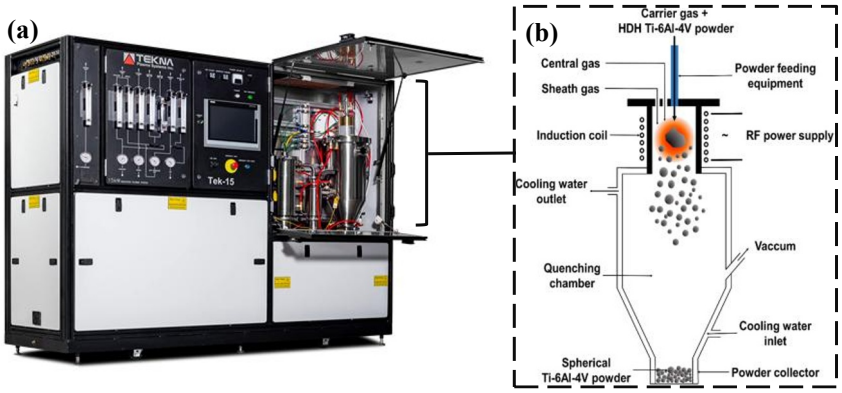

Fig. 1. (a) Tekna RF plasma system [28], (b) RF spheroidization process [8].

For each process parameter variation, the corresponding spheroidicity value was determined. The "spheroidization ratio", denoted as the number of spherical particles to the total number of particles in the treated product, was estimated by counting the spherical particles within a specific frame of the optical micrograph. Partly melted or elliptical-shaped particles were not counted as spherical particles.

Table 2. Operating conditions for the plasma spheroidization of Ti64 Grade 23 powder.

Parameter	Value
Plasma power, *kW*	10-15
Particle size, *μm*	25-125
Chamber pressure, *kPa*	65
Central gas flow rate (Ar), *slpm*	15
Sheath gas (Ar + He), *slpm*	45
Carrier gas flow rate (Ar), *slpm*	2
Powder feeding rate, *kg/h*	1

It should be noted that while particle size and plasma power varied, the total gas flow, the powder feed rate, and the carrier gas flow rate remained constant. Table 2 lists the average operating conditions for the plasma treatment of Ti64 powder. To ensure reliability and repeatability, experimental runs were conducted three times.

2.2 Computational data generation

A CFD model was developed using the 2024 R1 version of the ANSYS Fluent simulation software to generate computational data for the spheroidization of Ti64 Grade 23 powder. The initial step was designing a computational domain geometry of the RF plasma system, as depicted in Figure 2(a). In this 3-D geometry, a finite volume was created within the RF torch to act as a plasma generation energy source. The entire computational domain was then discretized through the meshing process, generating 500,201 cells. Figure 2(b) depicts the meshed cross-sectional area of the computational domain.

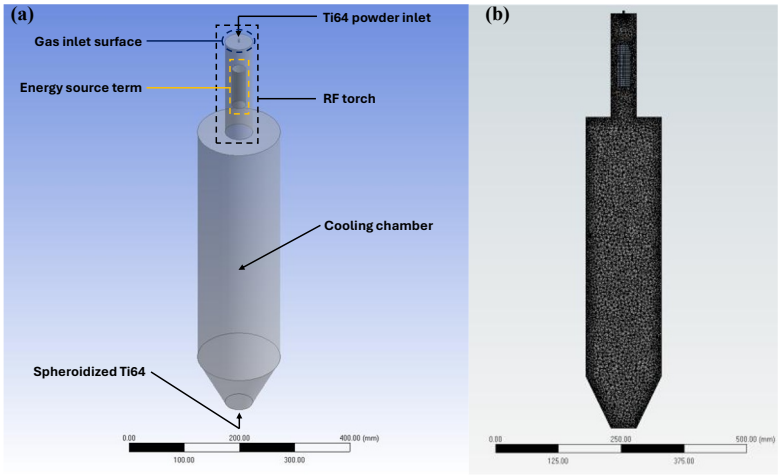

Fig. 2. (a) RF plasma system computational domain, (b) meshed cross-sectional area.

A converged numerical solution was reached by solving a set of governing equations for each cell intersection point. These equations were formulated by setting appropriate assumptions for the plasma flow field and particle behavior. Assumptions for the plasma flow field included the following considerations: (i) the plasma temperature field can be described as being optically thin and at local thermodynamic equilibrium (LTE) [29, 30]; (ii) the k-epsilon model is detailed enough to depict turbulence [31]; and (iii) viscous dissipation is negligible [32]. Similarly, the following assumptions were formulated for particle behavior: (i) particles are spherical and have a mono-diameter size distribution [17]; (ii) particle motion does not influence the plasma flow field [16]; (iii) the only forces affecting particle motion are the drag force, thermophoretic force, and gravity [15]; (iv) a Lagrangian method can be used to solve the discrete phase [31]; and (v) particles only receive heat from the plasma through convection. Radiation is neglected [15].

Based on the above assumptions, equations for the conservation of mass, motion, and energy were formulated. They are extensively discussed in [33-35]. In addition, it was determined that mathematical expressions such as Maxwell's equations should be included to account for the presence of an electromagnetic field in the RF plasma torch [36]. However, electromagnetic effects were ignored for simplicity, and instead, an energy source term was used for plasma generation. As for particles, their trajectories through the plasma stream were estimated by balancing the forces exerted on them, as shown in Equation 1 [31]:

$$m_p \frac{du_p}{dt} = C_D \frac{1}{2} \rho \left(\frac{1}{4}\pi d_p^2\right)(u - u_p)|u - u_p| + F_{th} + m_p g + m_p F_b(t) \quad (1)$$

where u, u_p, m_p, C_D, ρ, ρ_p, d_p, F_{th}, and $F_b(t)$ are respectively, the velocity of the gas, the particle velocity, the mass of the particle, the drag coefficient, the gas density, the particle density, the diameter of the particle, the thermophoretic force, and the Brownian force.

Energy balance on the particle allowed the quantification of the heat transferred from the plasma gas to the particle, as shown in Equation 2 [18, 37]:

$$Q_T = h\pi d_p^2 (T - T_p)\tau \quad (2)$$

where h, d_p, τ, T, and T_p are, respectively, the convective heat transfer coefficient, the particle diameter, the particle residence time, the gas temperature, and the particle

temperature. To calculate the heat transfer coefficient, h, the Nusselt number correlation, Nu, is used [31]:

$$Nu = \frac{hd_p}{k} = 2.0 + 0.6Re_d^{1/2}Pr^{1/3} \quad (3)$$

where k, Pr, and Re_d are the thermal conductivity, the Prandtl number, and the Reynolds number as a function of the relative velocity and the particle diameter, respectively. The heat, Q_M, required for a particle to melt completely, was calculated using Equation 4 [15, 38]:

$$Q_M = \frac{1}{6}\pi d_p^3 \rho_p \left[C_p(T_m - T_a) + H_f\right] \quad (4)$$

In this equation, C_p, T_m, T_a, and H_f are the specific heat, the melting temperature, the ambient temperature, and the latent heat of fusion, respectively. Finally, based on the principle of equivalence between the energy efficiency and the spheroidization efficiency, proposed by N.M. Dignard and M.I. Boulos [39], spheroidicity in terms of percentage, $S(\%)$, was calculated for all simulation runs. It was mathematically defined as the ratio of the energy transferred from the plasma gas to the particle, Q_T, over the heat required for complete melting, Q_M, multiplied by an experimentally determined system efficiency factor, η:

$$S(\%) = \eta\left(\frac{Q_T}{Q_M}\right) \times 100 \quad (5)$$

2.3 Feedforward neural network development

An ANN can be defined as a mathematical model able to elucidate statistical correlations between process parameters and output variables [40]. Mathematically, it can be expressed as [41]:

$$y_{calc} = f(\vec{x}) \quad (6)$$

where y, $\vec{x}$, and f are the output variable, the process parameters, and a factor called the response surface. y_{calc} would be considered a vector in the case of a multivariate output. In this study, spheroidicity is the model output, while process parameters are particle size, plasma power, gas flow, and powder feed rate. The combined experimental-computational dataset, with spheroidicity surface responses for each process parameter variation, was used to train the ANN model. The exceptional ability ANNs have to learn patterns within a dataset is not limited to linear relationships between input parameters and the desired output; it also extends to non-linear correlations [42].

There are several types of neural networks based on their architecture, learning method, and data processing technique. The ability of an ANN to detect patterns within a particular dataset heavily depends on the selected architecture [43, 44]. In this study, a feedforward neural network (FFNN), also called a multilayer perceptron (MLP), was developed for predicting Ti64 Grade 23 powder spheroidicity. The model architecture consisted of an input layer with four nodes corresponding to the four process parameters, a hidden layer of 4-12 nodes, and an output layer with a single node representing spheroidicity.

The 67 samples combined dataset was exported to a Google Colab notebook, where a PyTorch code was written to develop the above model architecture and launch the training process. Some of the most important parameters set to facilitate the training process included the ReLU and linear activation functions, respectively, for the hidden and output layers. The Adam optimizer, with a 0.001 learning rate, was selected as the optimization algorithm. Meanwhile, the number of epochs was set at 1000. Finally, to evaluate the model

performance, the following evaluation metrics were introduced: mean absolute error (MAE), mean squared error (MSE), and R-squared score (R2).

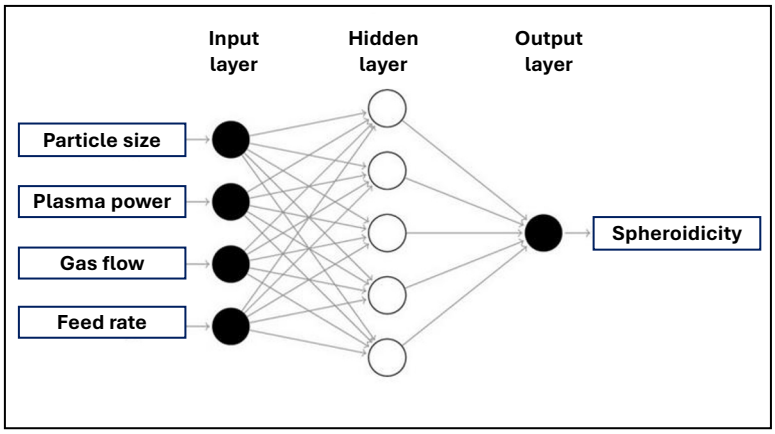

Fig. 3. Feedforward neural network architecture.

3 Results and discussion

3.1 Simulation results

3.1.1 Plasma flow field and particle trajectory

Key simulation results, generated using the CFD-pot processing unit in ANSYS Fluent, are presented in Figure 4. Figure 4(a) shows the static temperature distribution of argon gas throughout the entire computational domain, from the RF torch to the spheroidization reactor. In the RF torch, the formation of a high-temperature (~4000 K) plasma jet around the centerline can be observed.

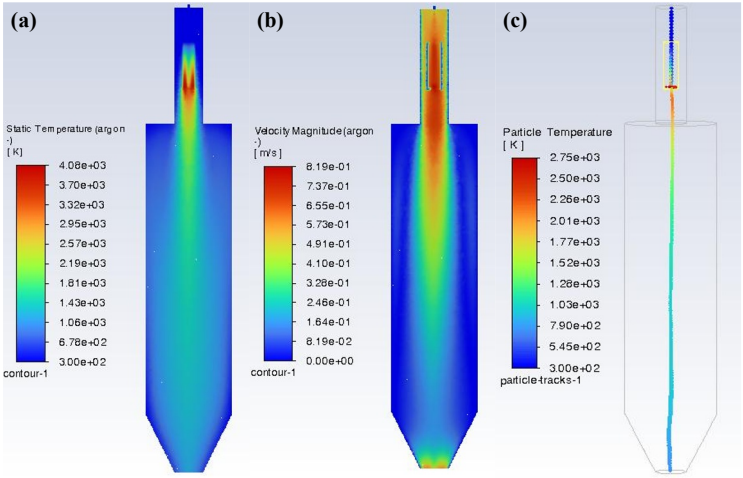

Fig. 4. (a) Temperature distribution, (b) velocity distribution, (c) particle trajectory and thermal history.

Further observation reveals a gradual temperature decrease as the plasma jet travels towards the reactor exit. The plasma formation characteristics and temperature decay profile closely mirror those reported by A. Seya *et al* [18]. Temperature decay occurs due to heat dissipation via conduction, convection, and radiation [39]. However, radiation was not incorporated into this model.

On the other hand, Figure 4(b) depicts the velocity distribution of argon gas as it enters through the torch inlet, passes through the high-temperature zone, and carries the injected powder particles through the reactor. While the gas reaches a maximum velocity of 0.8 m/s around the plasma core, a considerable gradient is observed as the gas moves away from the high-temperature region due to gas expansion and interaction with the surrounding environment [16].

As for Figure 4(c), it illustrates the tracked trajectory and thermal history of the injected Ti64 particles. It can be observed that the particles rapidly heat up as they enter the high-temperature plasma jet, reaching a temperature of 2750 K. This temperature should be sufficient to ensure complete melting, provided that the required residence time is met, as the melting temperature range of Ti64 is 1877–1933 K [45]. After passing through the high-temperature plasma core, where melting and spheroidization occur, particles cool down as they move toward the reactor exit. The trajectory and thermal profile exhibited by particles in this study align well with the findings of H. Zhu *et al* [46].

These simulation results provide valuable insights into the process dynamics, which would be difficult to observe through experimentation alone. The predicted gas and particle temperature fields are of utmost importance, as they enable calculating the amount of heat transferred from the gas to the discrete phase, using Equation 2. Without this, determining the spheroidicity percentage, as shown in Equation 5, would not be possible. Furthermore, understanding the heating and cooling rates that affect the final particle morphology depends on a deep knowledge of particle temperature trajectories [15].

3.1.2 CFD model validation and data expansion

In Figure 5, experimental and simulated spheroidicity values are compared to assess the accuracy and reliability of the model. Figure 5(a) illustrates how both the experimental and simulation spheroidicity trends increase as the plasma power rises from 10 to 15 kW. However, an inverse relationship is observed in Figure 5(b), where spheroidicity decreases as particle size increases from 25 to 125 µm. Whether these trends align with findings in the literature will be discussed in the sensitivity analysis section (point 3.3). In the current section, the focus remains on how closely CFD-generated predictions match experimentally measured values.

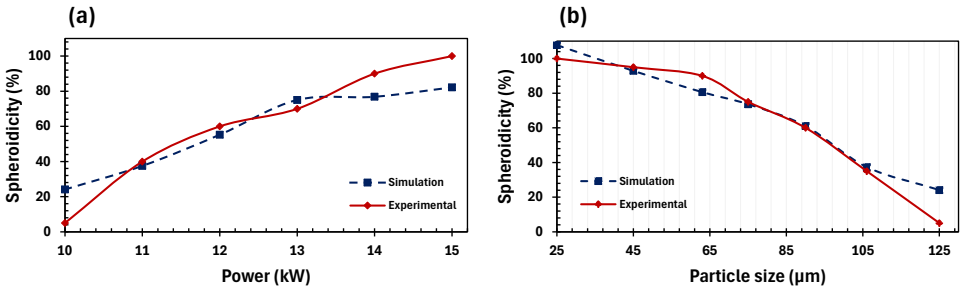

Fig. 5. (a) Spheroidicity vs power at dp = 125 µm, (b) spheroidicity vs particle size at P = 10 kW.

An investigation into Figures 5(a) and 5(b) reveals that, overall, for most variations in process parameters, the simulation and experimental spheroidicity are closely aligned.

However, some discrepancies can be noted. The CFD model appears to overestimate spheroidicity at low power (<10 kW) and large particle sizes (>106 µm) by 10-15 percentage points, while underestimating spheroidicity at high power (>13 kW). Several factors related to spheroidicity determination may explain these discrepancies.

Although deviations caused by potential human error while interpreting optical images could be a contributing factor, they are likely negligible compared to discrepancies originating from the CFD simulations. The CFD model made assumptions to simplify the process. For instance, radiation heat transfer was not accounted for. Additionally, for plasma generation, an energy source term was used instead of modeling the electrical arc itself, as was done by H.A. Gabbar *et al*, and H. Bahouh *et al* [30, 32]. Finally, while calculating spheroidicity based solely on the ratio of energy transfer to melting/spheroidization energy is a reasonable approximation, it does not fully capture the complex fluid dynamics within molten particles. Nevertheless, while the model may warrant some improvements, observed discrepancies represent less than 20% of the dataset. Moreover, the model captures well the general trends. Therefore, the level of agreement achieved is deemed acceptable to generate additional data points, incorporating parameter variations for all four process variables (plasma power, particle size, gas flow, feed rate).

3.2 Effect of training dataset size on model performance

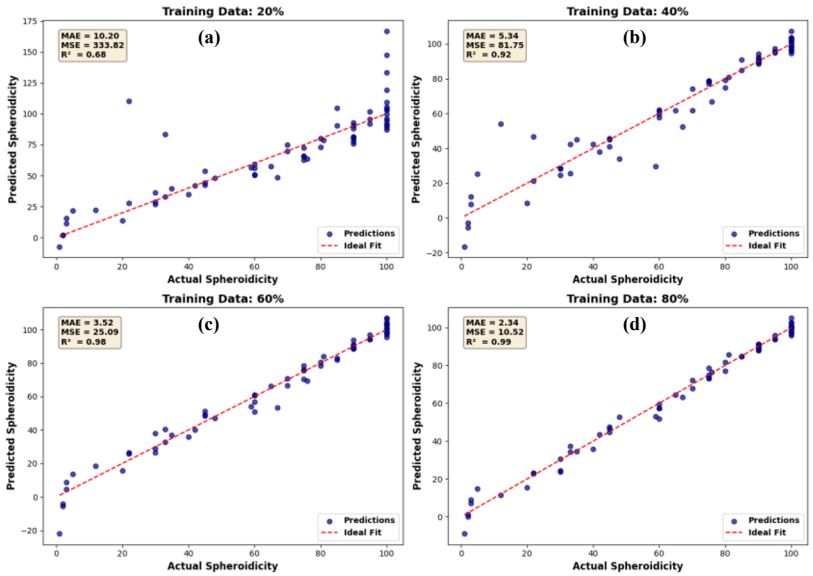

Fig. 6. Neural network regression analysis for training data sizes of: (a) 20%, (b) 40%, (c) 60%, (d) 80%.

Figure 6 illustrates the neural network model performance in predicting Ti64 powder spheroidicity across four different training set proportions (20%, 40%, 60%, and 80% of the whole dataset). In each of the four scatter plots, actual spheroidicity values from the combined experimental-computational (x-axis) dataset are compared to ANN predictions (y-axis). Comparison is based on the MAE, MSE, and R^2 evaluation metrics.

In Figure 6(a), 20% of the dataset, approximately 16 samples, is used for training. With an MAE of 10.20, an MSE of 333.82, and an R^2 value of 0.68, the scatter plot exhibits a significant deviation from the fitted line. This suggests that due to the small training dataset, the model struggles to fully capture patterns, and predict spheroidicity for unseen data. This observation aligns with conclusions made by L. Lin *et al* [47]. On the other hand, as the

training dataset increases from 20% to 40%, and further to 60% and 80%, it is observed that the MAE and the MSE drop significantly, implying reduced errors. Inversely, R^2 increases as the training dataset is increased, reaching successive values of 0.92, 0.98, and 0.99. These trends demonstrate that expanding small experimental datasets into larger datasets, by the addition of simulated data points, improves the neural network's ability to generalize and make accurate predictions [48].

However, training on 80% of the dataset only improved R^2 from 0.98 to 0.99 when compared to the performance of the 60% training dataset. This could lead to potential overfitting, as an overly complex ANN may fit errors in measurement or the noise [49]. Therefore, a training proportion close to 60% appears to be sufficient to reach good model generalizability, with significantly reduced errors.

3.3 Sensitivity analysis

3.3.1 Effects of particle size and plasma power on spheroidicity

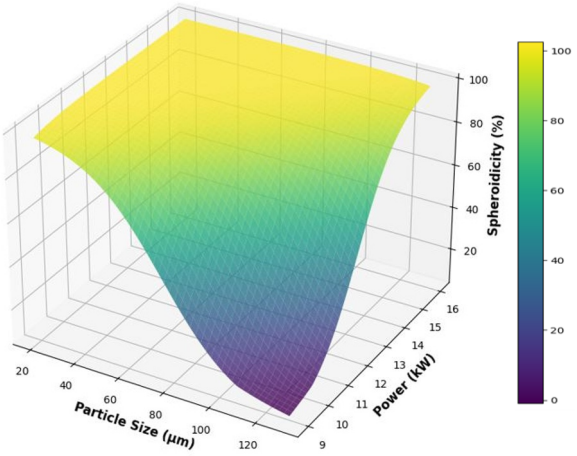

Fig. 7. Spheroidicity response surface vs particle size and plasma power (*plotted on Google Colab notebook using PyTorch code*).

Figure 7 presents a 3D response surface of the predicted Ti64 powder spheroidicity, expressed in %, as a function of particle size (μm) and plasma power (kW). This surface is generated using the developed FFNN model, which has established statistical correlations between the two inputs and the resulting spheroidicity, through training on the hybrid experimental-CFD dataset. Thus, the 3D surface plot provides an understanding on how varying particle size and plasma power simultaneously affect powder spheroidicity.

Investigation into particle size general behavior reveals that small particle sizes (20-40 μm) result in high spheroidicity, close to 100%. However, as particle size increases, a gradual decrease in output spheroidicity can be observed, in such a way that large particles tend to exhibit low spheroidicity. This is consistent with the fact that smaller particles require less energy to fully melt and spheroidize [15, 18, 50]. Inversely, as plasma power increases, spheroidicity increases as well. This could be explained by the fact that as the plasma power rises, it generates higher plasma temperature, and subsequently a larger and more intense heat transfer zone, providing more energy to particles for melting and spheroidization [11, 51].

Looking at the combined effect of particle size and plasma power, it can be observed that as particle size increases, the minimum power required to achieve a given spheroidicity rises sharply. For instance, 60 μm powders require a plasma power $\geq$ 12 kW to exceed 90%

spheroidicity, whereas 120 µm powders require a plasma power ≥ 15 kW, to achieve spheroidicity above 85%. In summary, the 3D surface plot indicates that achieving high spheroidicity for larger particles requires significantly higher plasma power compared to smaller particles.

3.3.2 Effects of gas flow and powder feed rate on spheroidicity

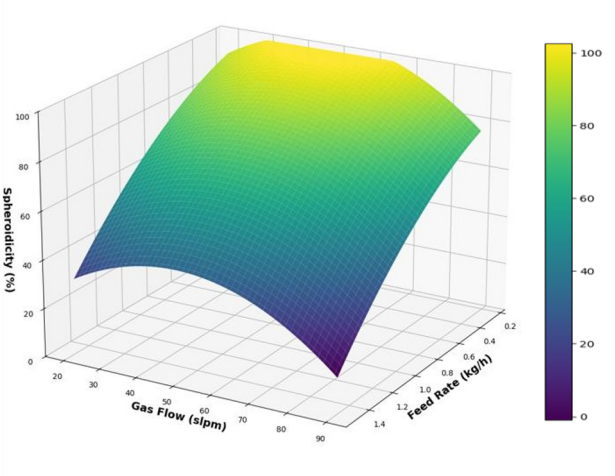

Fig. 8. Spheroidicity response surface vs gas flow and powder feed rate (*plotted on Google Colab notebook using PyTorch code*).

Figure 8 presents a 3D response surface of the predicted Ti64 powder spheroidicity, expressed in %, as a function of the powder feed rate (kg/h) and plasma gas flow rate (slpm). Similarly to the 3D surface plot in Figure 7, this plot was generated using the trained FFNN model.

The first observation is that, in general, increasing the powder feed rate contributes to a sharp decrease in the predicted spheroidicity. This drop in spheroidicity could be explained by the fact that, as the powder feed rate is increased, there is a higher concentration of particles entering the plasma jet. This leads to insufficient heat energy for all particles, coupled with increased particle-particle interactions, thus reducing energy transfer per particle. Moreover, due to the higher feed rate, particles' residence time inside the plasma jet is shortened, leading to limited melting and the inability for particles to fully spheroidize [18, 39, 52]. However, it is worth noting that though the plotted 3D spheroidicity plot does not reflect it, very low powder feeding rates could lead to low apparent density and poor flowability as a result of excessive heat available per particle [53].

As for the effect of gas flow rate on spheroidicity, it exhibits parabolic behavior. Spheroidicity seems to increase when gas flow is initially increased from 20 to 50 slpm. This is most probably due to low gas flow rates not being able to transfer enough heat to the powder particles. However, as gas flow is further increased from 50 to 90 slpm, spheroidicity gradually decreases. This is attributed to the higher flow rates causing particles to traverse the hot plasma region more rapidly, thereby decreasing their residence time, time, resulting in lower melting fraction and poor spheroidization [54]. These two contrasting trends for the same process parameter suggest that there should be an optimal range to maximize spheroidicity. H. Hou *et al* [14] reached the same conclusion when they evaluated the spheroidization rate under three different flow rates, respectively 35, 40, and 45 slpm. The middle flow rate, 40 slpm, yielded the highest spheroidicity value.

Investigating the combined effect of gas flow and powder feed rate reveals that there is a moderate combination of gas flow (40-60 slpm) and powder feed rate (0.6-1.0 kg/h) that produces maximum spheroidicity (90-100 %)

4 Conclusion

This study aimed to develop a hybrid experimental-computational method to predict the spheroidicity of Ti64 Grade 23 powder. This was achieved by combining a limited set of experimental data with a computational dataset, generated from a validated CFD model. The combined dataset helped address the challenge arising from data scarcity, which is inherent to many experimental studies. In addition, data from the combined dataset was used to train a feedforward neural network. As a result of this training, the FFNN demonstrated its advanced ability to learn patterns and correlations between the process parameters and the spheroidicity. The significance of the data augmentation technique lies in its contribution to improving the FFNN performance. Furthermore, sensitivity analysis was performed through 3D surface plots, revealing optimal processing conditions. It also allowed a vital understanding of the individual and combined effects of process parameters. Implications for the RF spheroidization process are quite substantial, as the developed FFNN stands as an appealing and powerful tool to drive the AM industry towards more controlled processes and the production of highly spherical metal powders, particularly Ti64 Grade 23 powder.

The authors wish to express their gratitude to the Department of Science and Innovation (DSI) for the financial backing provided through the Advanced Materials Initiative (AMI) and the South African Nuclear Energy Corporation (Necsa). They also appreciate the Research and Innovation Division at Necsa for granting access to their facilities. Special thanks are extended to the Necsa staff members, Mr. M.M. Makhofane and Mr. P.C. Smith, for their support with the plasma experiments.

References

1. A.H. Alami*, et al.*, Additive manufacturing in the aerospace and automotive industries: Recent trends and role in achieving sustainable development goals. Ain Shams Eng. J. **14**, 1-18 (2023) https://doi.org/10.1016/j.asej.2023.102516
2. H.A. Colorado, C.A. Cardenas, E.I. Gutierrez-Velazquez, J.P. Escobedo, S.N. Monteiro, Additive manufacturing in armor and military applications: research, materials, processing technologies, perspectives, and challenges. J. Mat. Res. Technol. **27**, 3900-3913 (2023) https://doi.org/10.1016/j.jmrt.2023.11.030
3. L. Chen, N.P.H. Ng, J. Jung, S.K. Moon, Additive Manufacturing for Automotive Industry: Status, Challenges and Future Perspectives, in Proceedings of the IEEE International Conference on Industrial Engineering and Engineering Management. 2023. Singapore (2023)
4. Y. Xu*, et al.*, Experimental analysis of the multiaxial failure stress locus of commercially pure titanium at low and high rates of strain. Int. J. Impact Eng. **170**, 1-17 (2022) https://doi.org/10.1016/j.ijimpeng.2022.104341
5. P. Muthuswamy, Influence of powder characteristics on properties of parts manufactured by metal additive manufacturing. Lasers Manuf. Mater. Process. . **9**, 312-337 (2022) https://doi.org/10.1007/s40516-022-00177-3
6. F.A. Talebi*, et al.*, Spreadability of powders for additive manufacturing: A critical review of metrics and characterisation methods. Particuology. **93**, 211-234 (2024) https://doi.org/10.1016/j.partic.2024.06.013

7. A.S. Tehrani, M.H. Korayem, S. Shao, M. Haghshenas, N. Shamsaei, Ti-6Al-4V powder characteristics in laser powder bed fusion: the effect on tensile and fatigue behavior. Addit. Manuf. **51**, (2022) https://doi.org/10.1016/j.addma.2021.102584
8. J. Li, Z. Hao, Y. Shu, J. He, Fabrication of spherical Ti-6Al-4V powder for additive manufacturing by radio frequency plasma spheroidization and deoxidation using calcium. J. Mat. Res. Technol. **9**, 14792-14798 (2020) https://doi.org/10.1016/j.jmrt.2020.10.054
9. Ji., L., C. Wang, W. Wu, C. Tan, G. Wang, X.-M. Duan, Spheroidization by Plasma Processing and Characterization of Stainless Steel Powder for 3D Printing. Metall. Mater. Trans. A. **48**, 4831-4841 (2017) https://doi.org/10.1007/s11661-017-4240-5
10. L.A. Dobrzanski, L.B. Dobrzanski, A.D. Dobrzanska-Danikiewicz, M. Kraszewska, Manufacturing powders of metals, their alloys and ceramics and the importance of conventional and additive technologies for products manufacturing in Industry 4.o stage. Arch. Mater. Sci. Eng. **102**, 13-41 (2020) https://doi.org/10.5604/01.3001.0014.1452
11. N. Nkhasi, W.d. Preez, H. Bissett, Plasma spheroidization and characterisation of commercial titanium grade 5 powder for use in metal additive manufacturing, in Proceedings of the RAPDASA-RobMech-PRASA-AMI Conference. 2023. CSIR International Convention Centre in Pretoria, South Africa: EDP Sciences (2023)
12. X. Zhang, X. Hou, Z. Hao, P. Wang, Y. Shu, J. He, Research on Spheroidization of Tungsten Powder from Three Different Raw Materials. Materials. **15**, 1-12 (2022) https://doi.org/10.3390/ma15238449
13. Y.L. Li, T. Ishigaki, Spheroidization of Titanium Carbide Powders by Induction Thermal Processing. J. Am. Ceram. Soc. **84**, 1929-1936 (2001)
14. H. Hou, Z. Ji, Z. Xie, H. Jin, Spheroidizing mechanisms and simulation of spherical silica in Oxygen-Acetylene flame. Adv. Powder Technol. **29**, 789-795 (2018) https://doi.org/10.1016/j.apt.2017.12.018
15. J.B. Tong, X. Lu, C.C. Liu, Z.Q. Pi, R.J. Zhang, X.H. Qu, Numerical simulation and prediction of radio frequency inductively coupled plasma spheroidization. Appl. Therm. Eng. **100**, 1198-1206 (2016) https://doi.org/10.1016/j.applthermaleng.2016.02.108
16. L. Xin, Z. Lang-ping, Z. Bing, Z. Rui-jie, H. Xin-bo, Q. Xuan-hui, Simulation of flow field and particle trajectory of radio frequency inductively coupled plasma spheroidization. Comput. Mater. Sci. **65**, 13-18 (2012) https://doi.org/10.1016/j.commatsci.2012.06.008
17. J. He, L. Bai, H. Jin, F. Yuan, Optimization of tungsten particles spheroidization with different size in thermal plasma reactor based on numerical simulation. Powder Technol. **302**, 288-297 (2016) https://doi.org/10.1016/j.powtec.2016.08.067
18. A. Seya, A. Kolesnikov, J. Van Der Walt, H. Bissett, Simulation of the effect of evaporation and gas composition during plasma spheroidization, in Proceedings of the RAPDASA-RobMech-PRASA-CoSAAMI Conference. 2022. Somerset West, South Africa: EDP Sciences (2022)
19. B.L. Smith, The difference between traditional and CFD validation benchmark experiments. Nucl. Eng. Des. **312**, 42-47 (2017) https://doi.org/10.1016/j.nucengdes.2016.10.007
20. J. Slotnick*, et al.*, CFD Vision 2030 Study: A Path to Revolutionary Computational Aerosciences. (2014); Available from: ntrs.nasa.gov/citations/20140003093.
21. M.J. Berger, M.J. Aftosmis, D. Marshall, S.M. Murman, Performance of a new CFD flow solver using a hybrid programming paradigm. J. Parallel Distrib. Comput. **65**, 414-423 (2005)

22. G. Calzolari, W. Liu, Deep learning to replace, improve, or aid CFD analysis in built environment applications: A review. Build. Environ. **206**, 1-12 (2021) https://doi.org/10.1016/j.buildenv.2021.108135
23. S. Calcaterra, G. Campana, L. Tomesani, Prediction of mechanical properties in spheroidal cast iron by neural networks. J. Mater. Process. Technol. **104**, 74-80 (2000)
24. R.P. Cherian, L.N. Smith, P.S. Midha, A neural network approach for selection of powder metallurgy materials and process parameters. AI Eng. **14**, 39-44 (2000)
25. T.A. Choudhury, N. Hosseinzadeh, C.C. Berndt, Using Artificial Neural Network to Predict the Particle Characteristics of an Atmospheric Plasma Spray Process, in Proceedings of the 6th International Conference on Electrical and Computer Engineering 2010. Dhaka, Bangladesh (2010)
26. A. Safonova, G. Ghazaryan, S. Stiller, M. Main-Knorn, C. Nendel, M. Ryo, Ten deep learning techniques to address small data problems with remote sensing. Int. j. Appl. Earth Obs. Geoinf. **125**, 1-17 (2023) https://doi.org/10.1016/j.jag.2023.103569
27. Z. Karoly, J. Szepvolgyi, Plasma spheroidization of ceramic particles. Chem. Eng. Process. **44**, 221-224 (2004) 10.1016/j.cep.2004.02.015
28. Tekna, Teksphero-15: Plasma Powder Spheroidization. (2024) 2025; Available from: https://www.tekna.com/spheroidization-systems-teksphero-15.
29. J.-H. Oh, S.H. Gwon, T.-H. Kim, J.-Y. Sun, S. Choi, Synthesis of titanium boride nanoparticles and fabrication of flexible material for radiation shielding. Curr. Appl. Phys. **31**, 151-157 (2021) https://doi.org/10.1016/j.cap.2021.08.009
30. H.A. Gabbar, M. Aboughaly, V. Damideh, I. Hassen, RF-ICP Thermal Plasma for Thermoplastic Waste Pyrolysis Process with High Conversion Yield and Tar Elimination. Processes. **8**, 1-15 (2020) https://doi.org/10.3390/pr8030281
31. N.Y.M. Gonzalez, M.E. Morsli, P. Proulx, Production of Nanoparticles in Thermal Plasmas: A Model Including Evaporation, Nucleation, Condensation, and Fractal Aggregation. J. Therm. Spray Technol. **17**, 533-550 (2008) https://doi.org/10.1007/s11666-008-9209-x
32. H. Bahouh, S. Rebiai, D. Rochette, D. Vacher, M. Dudeck, Modelling of an inductively coupled plasma torch with argon at atmospheric pressure. Phys. Scr. **014008**, 1-4 (2014) https://doi.org/10.1088/0031-8949/2014/T161/014008
33. V. Frolov, D. Ivanov, V. Sosnin, Numerical simulation of high power RF-RF hybrid plasma torch, in Proceedings of the International Scientific Electric Power Conference. 2019. St. Petersburg, Russia: IOP Conf. Ser.: Mater. Sci. Eng. (2019)
34. D.V. Ivanov, S.G. Zverev, Mathematical Simulation of Processes in ICP/RF Plasma Torch for Plasma Chemical Reactions. IEEE Trans. Plasma Sci. **45**, 3125-3129 (2017) https://doi.org/10.1109/TPS.2017.2773140
35. K.J. Mbwebwe, A. Kolesnikov, I.J. Van der Walt, H. Bissett, Computational fluid dynamics evaluation of conditions before impact of particles in plasma spraying process. Suid-Afrik. tydskr. nat.wet. tegnol. **40**, 16-21 (2021) https://doi.org/10.36303/SATNT.2021cosaami.04
36. P. Lyu, M. Lai, Y. Song, Z. Xue, F. Fang, Sub-nanometer finishing of polycrystalline tin by inductively coupled plasma-assisted cutting. Front. Mech. Eng. 2023. **18**, 1-17 (2023) https://doi.org.10.007/s11465-023-0751-5
37. W.A. Seya, A. Kolesnikov, I.J. Van der Walt, H. Bissett, Impact of heat transfer on spheroidization of titanium alloys, in Proceedings of the Conference of the South African Advanced Materials Initiative. 2021. Virtual (2021)
38. Z. Hao*, et al.*, Preparation of spherical Ti-6Al-4V powder by RF induction plasma spheroidization combined with spray granulation. Powder Technol. **387**, 88-94 (2021) https://doi.org/10.1016/j.powtec.2021.04.021

39. N.M. Dignard, M.I. Boulos, Powder Spheroidization Using Induction Plasma Technology, in Proceedings of the International Thermal Spray Conference. 2000. Montreal, Quebec, Canada: ASM Thermal Spray Society (2000)
40. L.A.C.D. Filippis, L.M. Serio, F. Facchini, G. Mummolo, ANN Modelling to Optimize Manufacturing Process, in Advanced Applications for Artificial Neural Networks, A.E. Shahat, Editor. p. 201-225. (2018)
41. M. Leparoux, M. Loher, C. Schreuders, S. Siegmann, Neural network modelling of the inductively coupled RF plasma synthesis of silicon nanoparticles. Powder Technol. **185**, 109-115 (2008) https://doi.org/10.1016/j.powtec.2007.10.004
42. K. Premlall, L. Koech, D. Faurie, Sorption capacity evaluation of industrial flue gas mixture using South African coal seams: Conventional and ANN modelling. Unconv. Resour. **6**, 1-13 (2025) https://doi.org/10.1016/j.uncres.2025.100168
43. I. Sadrehaghighi, Artificial Neural Networks (ANNs) Applied as CFD Optimization Techniques, in CFD Open Series. p. 1-89. (2021)
44. V.V. Pozevalkin, I.V. Parfenov, A.N. Polyakov, Approximation of machine tool experimental thermal characteristics by neural network. J. Phys. Conf. Ser. **1399**, 1-7 (2019) https://doi.org/10.1088/1742-6596/1399/4/04418
45. S. Keaveney, A. Shmeliov, V. Nicolosi, D.P. Dowling, Investigation of process by-products during the Selective Laser Melting of Ti6Al4V. Addit. Manuf. **36**, (2020) https://doi.org/10.1016/j.addma.2020.101514
46. H. Zhu, X. Li, Q. Chen, Three-Dimensional Simulation and Experimental Investigation on Spheroidization of Stainless Steel Powders Using Radio Frequency Thermal Plasma. J. Mater. Eng. Perform. **31**, 6606-6616 (2022) https://doi.org/10.1007/s11665-022-06714-7
47. L.-S. Lin, Y.-S. Lin, D.-C. Li, Y.-H. Liu, Improved learning performance for small datasets in high dimensions by new dual-net model for non-linear interpolation virtual sample generation. Decis. Support Syst. **172**, 113996 (2023) https://doi.org/10.1016/j.dss.2023.113996
48. T. Linjordet, K. Balog, Impact of Training Dataset Size on Neural Answer Selection Models, in Advances in Information Retrieval. p. 828-835. (2019)
49. Himmelblau, D.M., Accounts of Experiences in the Application of Artificial Neural Networks in Chemical Engineering. Ind. Eng. Chem. Res. **47**, 5782-5796 (2008)
50. S. Chikosha*, et al.*, Spheroidization of Stainless Steel Powder for Additive Manufacturing. Metals. **11**, 1-15 (2021) https://doi.org/10.3390/met11071081
51. H. Bissett, I.J.v.d. Walt, Metal and alloy spheroidization for the Advanced Metals Initiative of South Africa, using high-temperature radio frequency plasmas. J. South. Afr. Inst. Min. Metall. **117**, 975-980 (2017) https://doi.org/10.17159/2411-9717/2017/v117n10a8
52. J.-S. Nam, E. Park, J.-H. Seo, Numerical Analysis of Radio-Frequency Inductively Coupled Plasma Spheroidization of Titanium Metal Powder Under Single Particle and Dense Loading Conditions. Met. Mater. Int., 1-10 (2019) https://doi.org/10.1007/s12540-019-00348-6
53. X.-P. Liu, K.-S. Wang, P. Hu, Q. Chen, A.A. Volinsky, Spheroidization of molybdenum powder by radio frequency thermal plasma. Int. J. Miner. Metall. Mater. **22**, 1212-1218 (2015) https://doi.org/10.007/s12613-015-1187-7
54. S. Kumar, V. Selvarajan, P.V.A Padmanabhan, S.P. Sreekumar, Spheroidization of metal and ceramic powders in thermal plasma jet: Comparison between experimental results and theoretical estimation. J. Mater. Process. Technol. **176**, 87-94 (2006) https://doi.org/10.1016/j.jmatprotec.2006.02.023